Journal of Manufacturing Processes 156 (2025) 398–410

Contents lists available at ScienceDirect

Journal of Manufacturing Processes

journal homepage: www.elsevier.com/locate/manpro

Numerical modelling of laser welding pool thermal-dynamics and dissimilar materials mixing of cast iron, carbon-steel and nickel-alloy wire for weld crack prevention

Renzhi Zhang [a], Daichi Nishimoto [a,b], Ninshu Ma [a,*], Fenggui Lu [c], Tetsuo Suga [a], Takayuki Tabuchi [b], Syuichi Shimada [b]

[a] Joining and Welding Research Institute, Osaka University, Japan
[b] JATCO Ltd, Japan
[c] Shanghai key Laboratory of Materials Laser Processing and Modification, Shanghai Jiao Tong University, China

ARTICLE INFO

Keywords:
Laser welding
Keyhole dynamics
Three dissimilar materials
Droplets transfer
Materials mixing

ABSTRACT

To understand the prevention mechanism of weld cracks induced in laser welding dissimilar materials, carbon steel and cast iron with a nickel-alloy filler wire, it is necessary to investigate the melting pool thermal dynamics, keyhole mechanism and dissimilar materials mixing. In this study, a novel three-dimensional computational fluid dynamics (CFD) modelling on transient tracking of keyholes, transfer of molten wire droplets, mixing of filler and base metals, welding groove, coupled with conventional model of heat transfer, surface tension and recoil pressure, was developed. The simulated molten pool geometry and temperature field were compared with the experimental results, which confirmed the accuracy of the developed numerical model. The numerical results revealed that the keyhole underwent periodic oscillation and partial collapse, during which entrapped vapor formed transient bubbles that later escaped through buoyancy. The molten wire droplets significantly affected the flow field and local temperature, temporarily weakening Marangoni convection and altering keyhole stability. The nickel-alloy material concentrated primarily on the surface, then flowed into welding pool. After solidification, a large amount (65–75 %) of the nickel-alloy material kept in the upper half of the weld metal and a small amount distributed in the lower half zone. These distribution characteristics supplied a graded transition layer between the two dissimilar base metals benefiting to weld crack prevention. This research provided quantitative evaluation in visualizing the in-situ dynamic phenomena of dissimilar materials for laser welding process optimization.

1. Introduction

Laser welding offers high precision, high efficiency, and excellent suitability for automation. Compared with conventional fusion welding methods, its high energy density enables deep penetration with minimal heat input, resulting in a narrow heat-affected zone and limited distortion. The process's high speed and non-contact nature make it well suited for robotic manufacturing. Furthermore, laser welding provides exceptional flexibility for joining various materials, including high-strength steels, aluminum, titanium, and numerous dissimilar metal combinations [1–4]. Owing to these advantages, it has been extensively applied in the automotive, aerospace, electronics, and medical industries [5]. Laser welding is characterized by complex physical phenomena occurring over short timescales and within small spatial regions, including keyhole formation and collapse, vigorous molten-pool flow and rapid melting and solidification [6]. These coupled thermal–fluid–metallurgical behaviors are difficult to observe directly, even using advanced diagnostics such as high-speed imaging or X-ray radiography [7]. As a result, the process remains highly sensitive to welding parameters and challenging to control experimentally.

With the development of computational techniques and high-performance computing, numerical simulation has become an essential tool for investigating these complex behaviors [8–11]. Early studies were based on simplified heat-conduction models that predicted only approximate temperature fields without fluid-flow effects [12–14]. Subsequently, CFD-based multiphase models have enabled detailed

* Corresponding author.
E-mail address: ma.ninshu.jwri@osaka-u.ac.jp (N. Ma).

https://doi.org/10.1016/j.jmapro.2025.11.054
Received 13 October 2025; Received in revised form 8 November 2025; Accepted 20 November 2025
Available online 28 November 2025

analyses of keyhole dynamics, molten-pool flow, and melting–solidification behavior. For instance, Lin, Wang, and Lu [15] developed a transient multiphase model to study keyhole dynamics and porosity formation, providing insights into the relationship between recoil pressure, surface tension, and keyhole stability. Similarly, whereas Huang and Xu [16] simulated bubble evolution and entrapment during solidification, emphasizing the role of eddy flow. To enhance the reliability of such models, high-speed imaging and synchrotron-based diagnostics have been increasingly combined with CFD for validation [17]. These techniques make it possible to directly capture the evolution of the weld pool during welding, thereby providing valuable data for validating numerical simulations.

The growing demand for lightweight design in electric vehicles has further increased the importance of advanced joining technologies. Welding is now frequently employed to replace bolted connections, reducing component count and overall vehicle weight. [18–20] The use of high-strength materials has also expanded research on dissimilar-metal joining, such as aluminum–copper and magnesium–steel combinations [21–24]. In numerical investigations, Huang and Wang [25] examined how mismatches in thermal properties between base metals lead to asymmetric molten pools and uneven mixing. Similarly, Ai and Dong [26] constructed a three-dimensional multiphase flow model to analyze asymmetry between Q235 low-carbon steel and 316 L stainless steel under keyhole laser welding, that demonstrated keyhole-induced molten pool dynamics enlarge the molten pool. M. Shehryar Khan et al. [27] investigated the effects of full focusing and defocusing of the laser beam on keyhole behavior and molten pool morphology. Wu, Ishida et al. [28] developed a paraxial hybrid plasma–MIG welding process for medium-thick high-strength steel plates with a butting gap. Their study showed that molten pool flow promoted downward Ni transport, leading to an inhomogeneous distribution with higher Ni concentration at the pool bottom. While previous studies have advanced understanding of dissimilar welding, most focus on base material properties or laser parameters. Less attention has been focused on molten filler droplet induced dissimilar metal welding.

In this study, an EV automobile differential unit is manufactured by laser welding carbon steel to cast iron with nickel-alloy welding wire to replace conventional bolting for improving the joint strength and reducing weight. However, if the unsuitable laser welding conditions were employed, the crack occurred in the weld metal shown in Fig. 1. Concerning the welding crack occurrence, we found that the distribution of the nickel-alloy in the welding metal is one of the vital factors for crack prevention.

Therefore, it is important to investigate the molten pool dynamics and materials mixing through the numerical simulation approach. A three-dimensional CFD model was established that considered the molten pool flow, keyhole morphology, and dissimilar metal mixing behavior. Particular attention was given to the distribution of nickel-alloy welding material within the pool, and numerical results were validated against experimental observation.

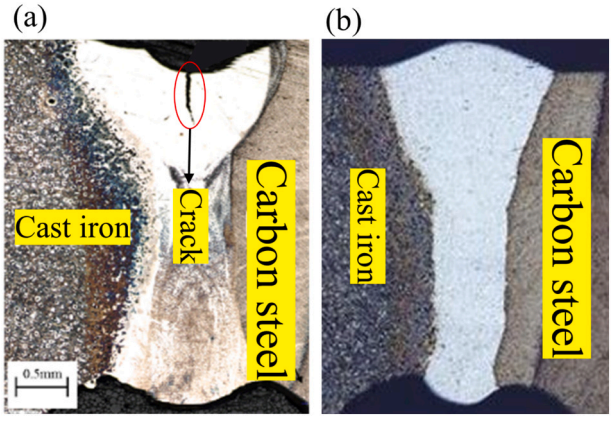

Fig. 1. Cross-sectional macrostructures of dissimilar welding between carbon steel and cast iron (a) No filler wire (b) With nickel-alloy filler wire.

2. Materials and methods

A differential unit was designed for a kind of electric vehicle. The ring gear, (carbon steel, Cr—Mn steel) and differential case (cast iron FCD600 equivalent) were joined by laser welding using a nickel-alloy filler wire (MG82, containing at least 72.12 % Nickel) [29]. The detailed chemical compositions were listed in Table 1. The welding configuration was a circular path with a radius of 56 mm, which contained a 0.4 mm width of the groove at the upper region of the base metals. The height of the base metal was 3.5 mm. A YAG laser oscillator provided the laser beam, which was perpendicularly to the base metal, with an output power of 2510 W and a 0.4 mm focal spot diameter, the focal position was right at bottom of base metal. The welding was performed along a circular path right at the groove position with the speed of 1.5 m/min [30]. The filler wire was fed at a speed of 2.6 m/min. The wire feeding position could be slightly shifted toward either the carbon steel or the cast iron side, as illustrated in Fig. 2. A centered configuration, shown in Fig. 2(a), corresponded to the wire aligned with the groove center. Since the offset of the wire was not the focus of this study, the case with the wire placed at the joint center was selected for analysis in the present work.

3. Numerical model

3.1. Geometry and meshing

In this study, a three-dimension CFD model was developed using ANSYS Fluent to simulate the dissimilar metal laser welding process. The dissimilar material welding involved highly complex thermophysical phenomena, including heat conduction, convection, radiation, metal evaporation, and the influence of molten droplet transfer. To improve computational efficiency and ensure numerical convergence, certain simplifications were made by neglecting minor effects that have little impact on overall calculation. Accordingly, the following assumptions were made in the present model.

(1) The molten pool metal was assumed as a laminar, incompressible Newtonian fluid.
(2) All material properties in the simulation were assumed to be solely temperature-dependent, with no chemical reactions occurring among different materials.
(3) The reflection of the laser beam within the keyhole was neglected. All forms of energy input, such as thermal radiation and multiple reflections, were incorporated into the model through an equivalent heat source.

Table 1
Chemical composition of Chrome-Manganese steel (carbon steel), FCD600 equivalent.

Chrome-Manganese steel		FCD600 equivalent		MG82	
C	0.27	C	3.7	C	0.036
Mn	1.27	Mn	0.51	Mn	2.95
Ni	0.07	Ni	–	Ni	72.12~
Cr	1.27	Cr	–	Cr	19.89
Cu	0.12	Cu	0.56	Cu	<0.005
Si	0.27	Si	2.36	Si	0.10
S	0.03	S	~0.02	S	<0.0005
P	0.015	P	~0.05	P	0.002
Ti	<0.01	Sn	~0.05	Ti	0.36
Al	<0.03	Mo		Nb	2.37
				Fe	1.32

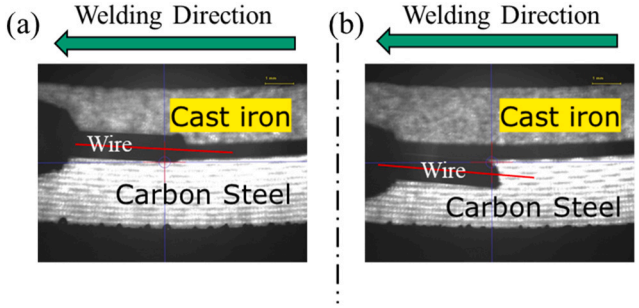

Fig. 2. Actual welding experiment procession (a) Wire position at groove center (b)Wire position at carbon steel.

(4) The total welding length in the experiment was 351 mm, while a 16 mm segment in the stable welding region was selected as the computational domain for the simulation.
(5) The impact of droplets on the weld pool was neglected.

Based on the assumption, a three-dimensional geometry model was built. The computational domain was constructed with an overall dimension of 16 mm (length) × 10 mm (width) × 4.6 mm (height), as illustrated in Fig. 3. The domain consisted of two main regions: the metallic fluid domain and the surrounding air domain. The metallic region, representing the welding zone and dissimilar base metal material, had a vertical height of 3.5 mm. The air region was divided into two layers: a 0.6 mm-thick top layer and a 0.5 mm-thick bottom layer, located above and below the metallic region, respectively.

Fig. 4 introduced the meshing model of the simulation. The entire computational domain was discretized with hexahedral elements. The average mesh size was approximately 0.1 mm. To enhance resolution near the weld pool and along the wire feeding path, local mesh refinement was applied in these regions. Conversely, mesh coarsening was implemented in areas distant from the melting zone, particularly near the domain boundaries to improve efficiency without significantly compromising accuracy. The final mesh consisted of approximately 324,000 elements.

3.2. Governing equations

The calculation was governed by the conservation equations of mass, momentum, and energy. These equations collectively described the evolution of fluid flow and temperature field in the welding process.

Mass conservation equation:

$$\frac{\partial(\rho\vec{u})}{\partial t}+\nabla(\rho\vec{u})=S_m \tag{1}$$

where ρ is the fluid density, u is the mean velocity in x, y, z direction, and S_m represents the source term, which is from the molten droplet material.

Momentum conservation equation:

$$\frac{\partial(\rho\vec{u})}{\partial t}+\rho(\vec{u}\cdot\nabla)\vec{u}=-\nabla P+\mu\cdot\nabla^2\vec{u}\cdot+\rho g+Fs \tag{2}$$

where P is the pressure, μ is the dynamic viscosity, and g is the gravitational acceleration. The source term Fs includes additional volume forces relevant to laser welding, contain recoil pressure at the keyhole wall and surface tension forces at the liquid–gas interface.

Energy conservation equation:

$$\frac{\partial(\rho h)}{\partial t}+\nabla(\rho\vec{u}h)=\nabla(k\nabla T)+S_q \tag{3}$$

where h is the enthalpy, T is the temperature, and k is the thermal conductivity. The source term S_q accounts for the laser heat input, molten droplet heat and latent heat associated with melting and solidification. To capture phase change, the enthalpy–porosity method is adopted:

$$h=\int c_p(T)dT+f_L\Delta L_m \tag{4}$$

where c_p is the specific heat, L_m is the latent heat of melting and f_L represents the liquid fraction, which governs the mushy zone resistance, allowing the proper transition between solid and liquid phases. f_L complied to be liner with temperature.

$$f_L=\begin{cases}0; & T\le T_S\\ \dfrac{T-T_S}{T_L-T_S}; & T_S\le T\le T_L\\ 1; & T\ge T_L\end{cases} \tag{5}$$

where T is the present temperature, T_S and T_L is the solidus, liquidus temperature respectively.

3.3. Laser heat source model

In this study, the total heat input was considered to consist of two parts: the energy absorbed directly from the laser beam, and the heat carried by molten droplet. Since the laser beam was applied perpendicularly to the base metal and irradiated directly into the bottom of the groove, multiple reflections inside the groove were neglected. To express the laser energy distribution, a rotating Gaussian distributed body heat source model was applied as shown in Fig. 5, the equation is written as follows:

$$q(x,y,z,t)=q_l e^{-6\left[\frac{(x-v_0t)^2+(y)^2}{r(z)^2}\right]} \tag{6}$$

$$q_l=\frac{9Q^*\eta}{\pi {R_0}^2 H} \tag{7}$$

where v_0 is the welding velocity, t is the practical welding time, H is the depth of heat source, R_0 is the radius on the upper surface of the heat

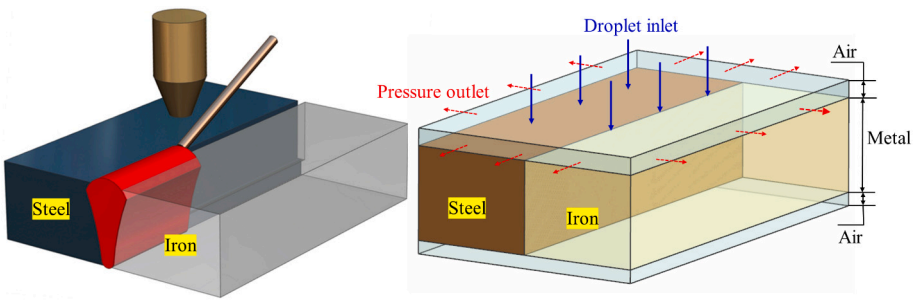

Fig. 3. Instruction schematic of welding process and Geometry model built.

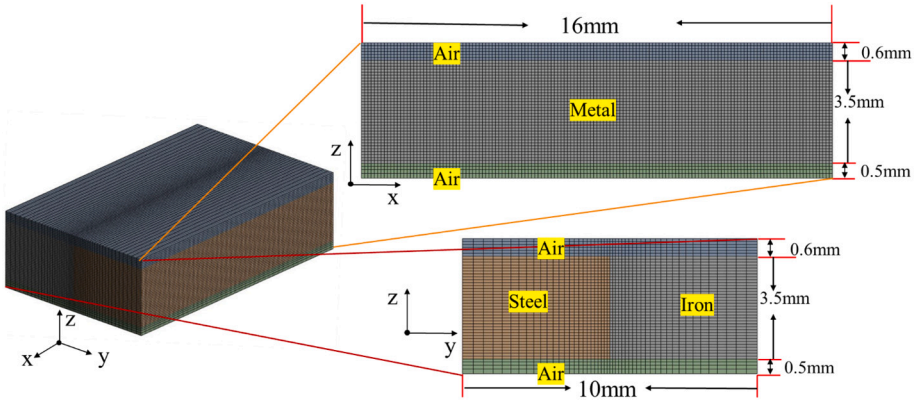

Fig. 4. Meshing of calculation model.

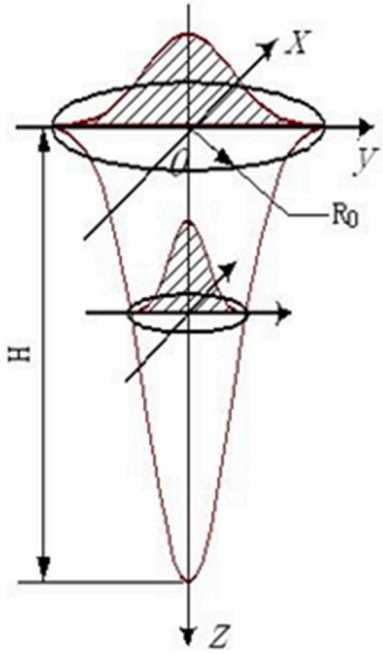

Fig. 5. The equivalent heat source model.

source, Q is the laser power input value and η is the laser absorption efficiency as shown in Table 2. Since the position of laser focal was at the bottom of the base metal, the laser spot diameter increased with the defocusing distance. Accordingly, the laser spot diameter distribution at depth direction can be expressed as:

$$r(z) = R_0\sqrt{ln\left(\frac{H}{z}\right)} \tag{8}$$

Table 2
Equivalent heat source parameters.

Property	Symbol	Value	Units
Laser input power	Q	2650	W
Weld velocity	v_0	25	mm/s
Welding time	t	–	s
Heat source depth	H	4.4	mm
Heat source radius at upper surface	R_0	0.6	mm
Laser absorption efficiency	η	0.95	–

3.4. Molten droplets model

In the experiment, the filler wire was placed on the front side of the laser beam and fed into the center of the groove shown in Fig. 6(a). In the numerical simulation, the wire feeding was represented by periodic molten droplet dripping above the molten pool as shown in Fig. 6(b). The volume of each molten droplet was determined based on the actual wire feeding rate and wire diameter, ensuring consistency between the experimental and numerical conditions. In this way, the discrete molten droplet model kept numerically stable and physically realistic.

The molten droplet dripping was controlled by a trigonometric function to mimic its periodic dripping behavior. The radius of the molten droplets and moving velocity was controlled by the equation:

$$r_d = \sqrt{(x - v_0 t)^2 + y^2} \tag{9}$$

where r_d is the molten droplet radius.

The molten droplet dripping condition was then governed by a sinusoidal function:

$$DC = \sin(2\pi \cdot D_n \cdot t) \tag{10}$$

where D_n represents the dripping number which is set as 100 droplets per second. A droplet was considered to enter the molten pool only when two criteria were simultaneously satisfied: the radial distance $r_d \leq 1mm$, and the sinusoidal function exceeded a threshold ($DC \geq 0.8$). Under these conditions, the dripping velocity was set to 0.143 m/s, otherwise, no molten droplet entry was allowed. The temperature of molten droplet was set as the melting point temperature of wire material (nickel-alloy) 1650 K.

3.5. Recoil pressure model

During laser keyhole welding, the evaporation of metal at the surface generates a recoil pressure that acts normal to the liquid–gas interface. In this study, the recoil pressure was expressed in an exponential form derived from the Clausius–Clapeyron [31] equation:

$$P_r = P_0 e^{\left(C\cdot\left(1-\frac{T_v}{T}\right)\right)} \tag{11}$$

where P_r is the recoil pressure, P_0 is the reference pressure constant, C is a material-dependent coefficient related to the latent heat of vaporization and the gas constant, T_v is the evaporation temperature of the material, and T is the local surface temperature.

3.6. Surface tension model

Surface tension is the interfacial force acting between the deposited

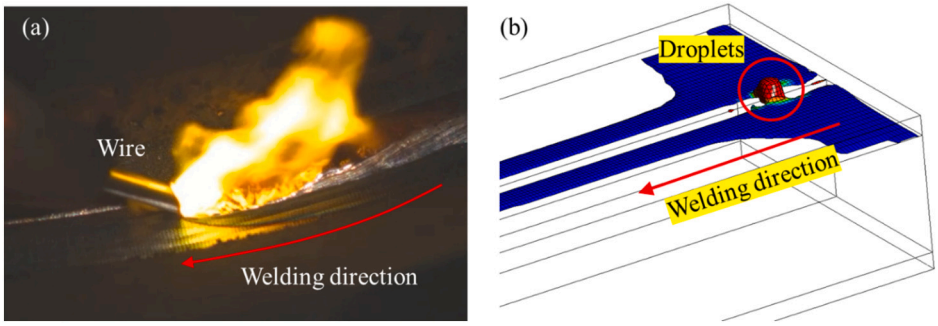

Fig. 6. Illustration of welding wire feeding (a) Wire feeding in the experiment (b) Molten droplet dripping model in the simulation.

metal and the surrounding air, and it plays a significant role in driving molten metal flow [32]. In this study, the Continuum Surface Force (CSF) model [33] was applied to simulate fluid flow induced by surface tension variations with temperature. Under this framework, the Marangoni force at the free surface can be described following the formulation proposed by Fan et al. [34].

$$\tau = \frac{d\gamma}{dT}\nabla_S T \tag{12}$$

where τ represents the shear stress, γ is the temperature dependent surface tension, $\nabla_S T$ refer to the surface gradient of temperature.

3.7. Volume of fluid model

The free surface of the keyhole and molten wire droplets were captured using Volume of fluid (VOF) method, which was expressed as follows:

$$\frac{\partial F}{\partial t} + F\nabla\vec{u} = 0 \tag{13}$$

where F is the volume fraction, which is between 0 and 1.

3.8. Initial conditions

In the numerical setup, the initial regions of the metals and groove were defined through initialization. The width of the groove was 0.35 mm and with a depth of 2.5 mm. Blow this 2.5 mm height, the two base metals were assumed to be in direct contact without a gap. The geometric instruction was as Fig. 7.

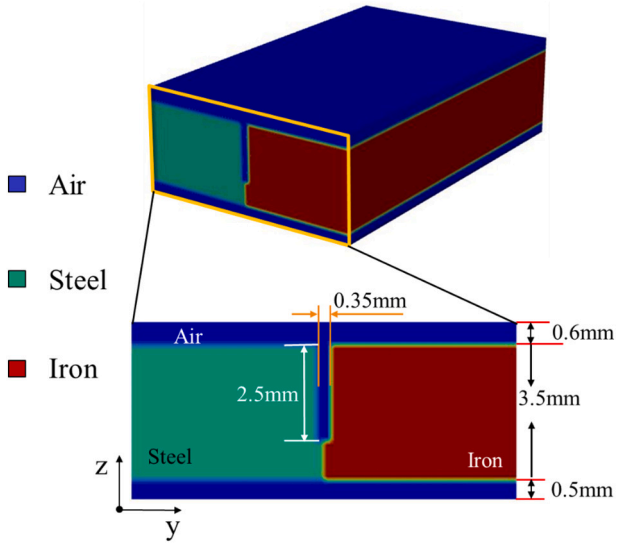

Fig. 7. Initial configuration of the base metal domain.

The initial temperature equals 300 K, which is the same as environmental temperature. Because the groove width was smaller than the laser spot diameter, the incident laser energy was primarily distributed within the groove. In the model, the laser beam was therefore interacted only with outer surfaces of the base metals, the groove sidewalls and the base metal blows the groove. This allowed the equivalent Gaussian volumetric heat source to be applied only to the base metal, not the air inside of the groove, as illustrated in Fig. 8. The calculated welding time was 0.5 s, which was 12.5 mm in length. After the welding calculation, a 0.2 s period naturally cooling procedure was also calculated.

3.9. Temperature-dependent material properties

To improve the accuracy of the numerical calculations, the key thermophysical properties of the three metals—density, viscosity, and surface tension—were experimentally measured. These properties were obtained over a range of temperatures relevant to the welding process and were used as temperature-dependent inputs for the CFD model. Accurate determination of these parameters was essential for capturing the molten pool flow behavior and surface deformation under Marangoni and recoil pressure effects. The experimentally measured temperature-dependent curves of density and viscosity for the three metals are presented in Fig. 9(a) and (b), respectively. The density decreased approximately linearly with temperature, whereas viscosity exhibits a nonlinear decline, indicating enhanced fluidity at elevated temperatures. The other relevant parameters used in the simulation are summarized in Table 3.

4. Results and discussion

4.1. Temperature distribution and molten pool shape evaluation

Fig. 10 presented a comparison between the experimentally observed cross-section and the numerically simulated molten pool profile. The experimental result showed a deeply, fully penetrated fusion zone extending into the groove and an asymmetric solidification boundary between the steel and cast-iron sides. The corresponding numerical result reproduced the overall pool shape, and the height and width of the molten pool are consistent with the experimental observation. The width of the upper surface of molten pool was 2.01 mm, while the simulation result showed a 1.9 mm width at upper surface, which indicated that the applied equivalent heat source accurately represented the laser energy distribution and absorption behavior during welding procession. This consistency demonstrated the applicability and reliability of the developed heat source model for predicting molten pool formation and thermal behavior in current study.

The temperature distribution along the welding direction at the molten pool surface was measured using an infrared thermal imaging camera, which was shown in Fig. 11(a). Three equally spaced points (A, B, and C) were selected for quantitative evaluation, where the time $t =$

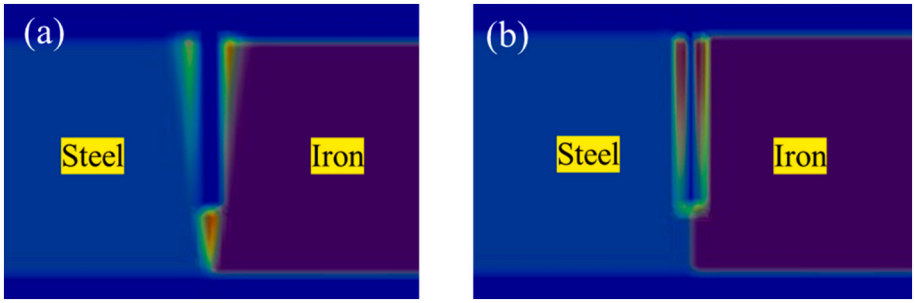

Fig. 8. Schematic of the initial heat source configuration (a) The heat source acted inside the metal (b) Heat source acted on the metal surface.

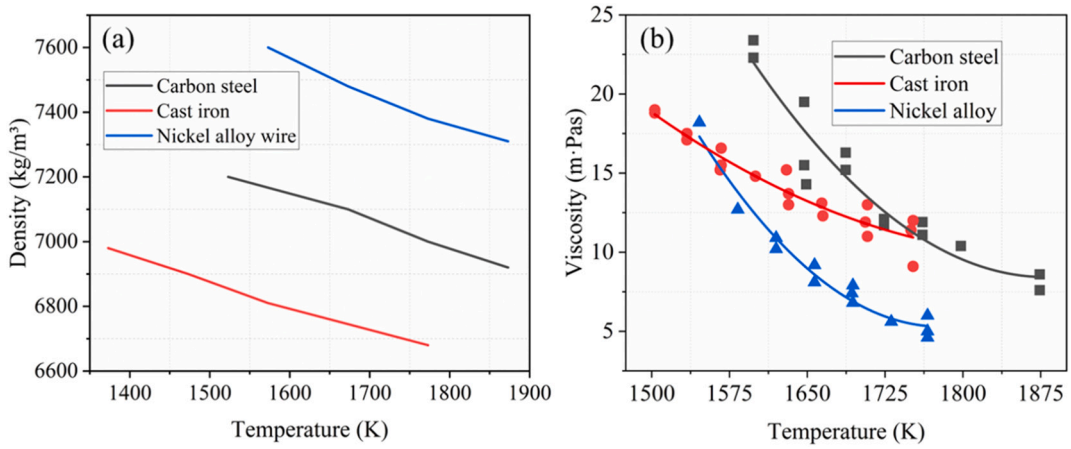

Fig. 9. Temperature-dependent thermophysical properties of carbon steel, cast iron, and nickel-alloy (a) Density (b) Dynamic viscosity.

Table 3
Temperature dependent material properties for each material.

Property	Chrome-Manganese steel	FCD600 equivalent	MG82	Units
Specific heat	455–1100	500–950	500–750	$J{\cdot}kg^{-1}{\cdot}K^{-1}$
Thermal conductivity	30–40	18–45	17–25	$W{\cdot}m^{-1}{\cdot}K^{-1}$
Solidus temperature	1580	1434	1540	K
Liquidus temperature	1623	1473	1600	K
Latent heat of melting	272,000	240,000	280,000	$J{\cdot}kg^{-1}$
Surface tension	1.74–1.8	1.42–1.6	1.72–1.8	$N{\cdot}m^{-1}$

0.0 s corresponded to the moment when the laser beam just passed directly over each point. In the numerical simulation shown in Fig. 10 (b), three points were selected according to the same spatial criteria as in the experiment to enable a direct comparison of temperature histories. Fig. 10(c) compared the experimental temperature measurements with the simulated results at the same locations. In the figure, "Exp" referred to the experimentally measured points, while "Sim" denotes the corresponding simulation results. The experimentally measured peak temperatures near the laser beam were found to be between 1500 K and 1700 K, decreasing gradually to about 1000 K approximately 0.5 s after the laser moved away from the observation point. The peak temperatures obtained from the simulation ranged between 1600 K and 1750 K, which was in close agreement with the experimental results. After approximately 0.5 s, the simulated temperatures decreased around 1100 K. Both the experimental and simulated results exhibited similar cooling rate trends. The simulated surface temperature is approximately 200 K higher than the experimental measurement. This discrepancy can

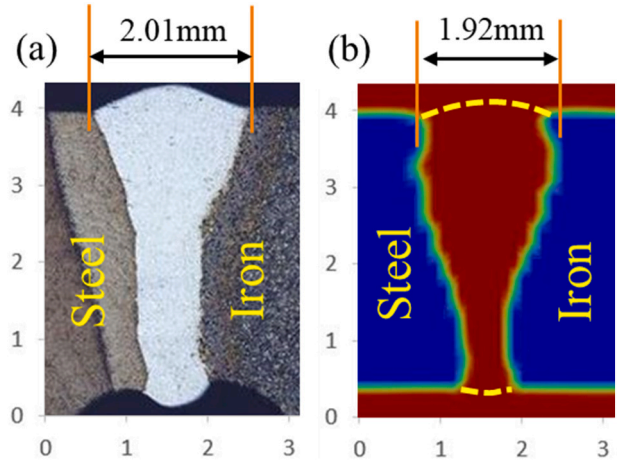

Fig. 10. Comparison of molten zone morphology between experiment and simulation (a) Experimental result (b) Simulated result.

be attributed primarily to the influence of the shielding gas flow during the experiments, which continuously removes heat from the molten pool surface. In the present simulation, however, the inflow and outflow of the shielding gas were neglected to simplify the computational model and improve efficiency. Overall, the calculated temperature evolution during the cooling process showed good agreement with the experimental observations, also confirming the reliability of the equivalent heat source model.

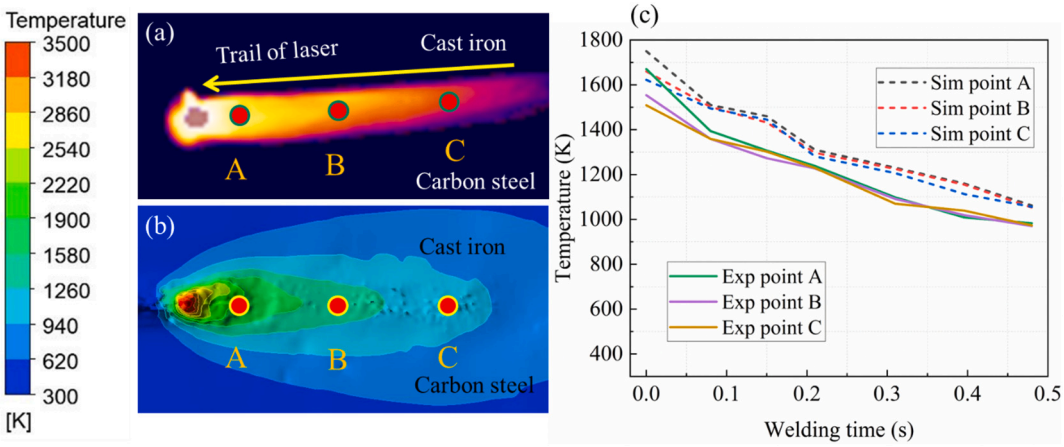

Fig. 11. Experimental and simulated curves comparing surface heat dissipation (a) Comparation of temperature field map in experiment (b) Comparation of temperature field map in simulation (c) Comparation of cooling temperature curve.

4.2. Dynamic keyhole behaviors

The dynamic behavior of the keyhole played an important role in determining molten pool stability, penetration depth, and defect formation such as porosity. In this section, the transient evolution of the keyhole during laser welding was analyzed. Fig. 12 (a ~ f) illustrated the transient evolution of the keyhole and molten pool geometry, showing both longitudinal section view and top-side view distributions of temperature and flow velocity vector. In the longitudinal view, the velocity vectors were displayed on the keyhole free surface and on a central plane extracted through the middle of the groove, representing the characteristic flow distribution within the molten pool. At the initial stage shown in Fig. 12(a), the laser irradiation rapidly melted the groove bottom, producing a shallow cavity due to recoil pressure. The molten metal was driven upward along the front wall and outward along the free surface, forming an unstable open keyhole. As the laser continued to irradiate shown in Fig. 12(b), the depth and width of keyhole extended along the welding direction, accompanied by a strong upward vapor flow and an opposing downward melt flow that established a closed circulation loop inside the molten pool. The velocity vectors at the keyhole surface were oriented nearly perpendicular to the keyhole wall, indicating an outward expansion trend of the molten metal. The top-view flow vectors revealed a Marangoni-driven circulation from the steel side toward the cast-iron side, producing asymmetric convection patterns consistent with the difference in thermophysical properties between the two materials.

In the subsequent stage shown in Fig. 12(c), the molten pool reached a quasi-steady state where the recoil pressure, surface tension, and hydrostatic forces reach a dynamic balance. Small-scale vortices were observed near the keyhole surface wall, suggesting periodic oscillation and “breathing” of the keyhole. Under this quasi-steady state of the keyhole, the metal fluid in the lower region of the pool flowed backward and upward along the rear wall, forming a recirculating flow pattern beneath the keyhole. This flow behavior resulted from the combination effects of recoil pressure acting on the keyhole bottom and Marangoni convection along the temperature gradient. The metal near the front wall was pushed downward by vapor recoil, while the fluid near the rear wall rose due to buoyancy and surface tension gradients, establishing a closed-loop circulation within the molten pool. This circulation not only stabilized the keyhole shape but also enhanced heat and material transfer inside the pool.

In Fig. 12(d ~ f), the molten pool gradually expanded toward the cast-iron side. The upward flow near the front wall became weaker, while the rear-wall vortex dominated the internal circulation, leading to slight fluctuation in the keyhole depth and shape. The top-surface temperature distribution evolved into an elongated elliptical profile aligned with the welding direction, and the asymmetric Marangoni flow continued to promote lateral transport of molten metal and alloying elements. During the oscillation of the keyhole, its periodic opening and collapse caused part of the vapor to be trapped beneath the keyhole bottom. As the keyhole closes, these entrapped gases remained within the molten pool, resulting in the formation of voids, as illustrated in Fig. 12(e) and (f).

Overall, the simulated results captured the complete formation, stabilization, and oscillation process of the keyhole. The dynamic interaction between recoil pressure and Marangoni convection was demonstrated to be the main mechanism governing keyhole morphology and molten-pool stability in dissimilar laser welding of carbon steel and cast iron.

4.3. Molten droplet transfer and mixing behavior

Fig. 13(a ~ e) presented the transient behavior of the first molten filler droplet dripping into the groove, showing both the cross-sectional and longitudinal views of the molten pool evolution. The blue region represented the interface between the air and the metallic surface, which visualized the groove morphology during the initial stage of welding, as shown in the cross-sectional views above. In the longitudinal section below, the side close to the observation plane corresponded to the carbon steel. As the groove bottom absorbed the laser energy the base metal melted into liquid, the original groove geometry gradually disappeared. The molten metal filled the region that was initially occupied by air at the bottom of the groove. Consequently, the air–metal interface vanished in this area, appearing as a white cavity in the longitudinal view. It should be noted that this white region did not represent an actual void or pore, rather, it indicated the zone where the molten metal has completely replaced the air because of local melting and flow. This phenomenon marked the transition of the base metal from the solid to the liquid state during the early welding stage, creating favorable conditions for subsequent droplet transfer and mixing within the groove. As the molten droplet approached the groove showed in Fig. 13(b), a portion of the groove wall and the metal at the groove bottom have been melted due to the intense laser irradiation.

When the molten droplet first contacted the molten pool in Fig. 13 (c), its thermal energy was rapidly transferred to the base metal, causing an instantaneous expansion of the molten pool and the local temperature near the impact region increased, a strong downward flow developed beneath the droplet, as shown in the longitudinal section. This impact also generated a pressure wave that propagated through the molten pool and slightly enlarged the molten pool.

With continued spreading, the molten droplet metal was entrained into the groove, promoting further melting of the near-edge region and

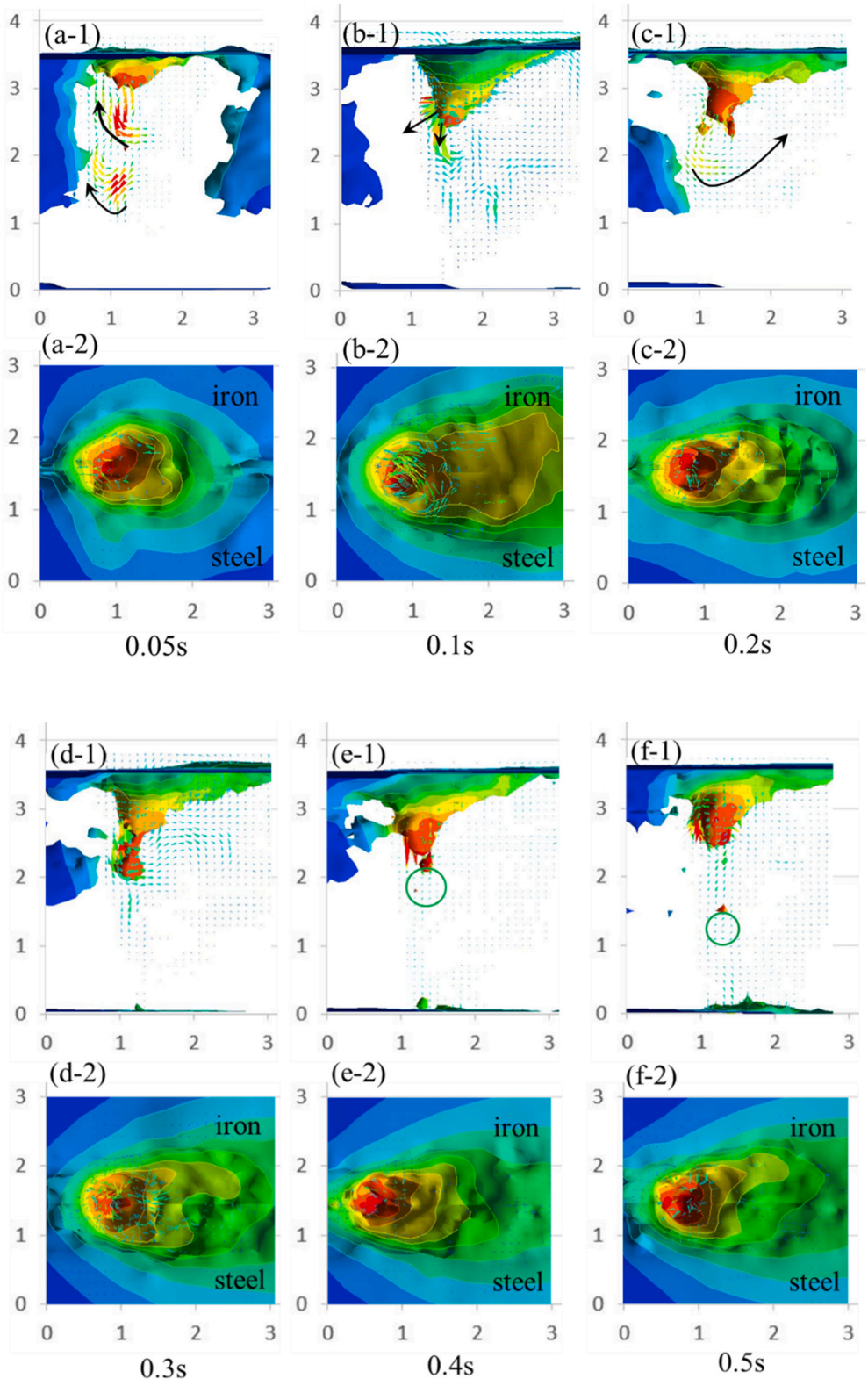

Fig. 12. Transient evolution of keyhole dynamics and molten pool flow: (a-1) ~ (f-1) Longitudinal section view; (a-2) ~ (f-2) Top view.

gradual reshaping of the groove profile shown in Fig. 13(d ~ e). The flow was mainly governed by inertia of molten droplet and then by Marangoni shear along the strong surface temperature gradient. Because a stable vapor channel has not developed at the very beginning of welding procedure, the recoil pressure was negligible, and no gas entrapment was observed at this stage. Instead, in the longitudinal view below, the nickel-alloy volume fraction highlights where the molten droplet first mixed with the molten base metal, discrete Ni-alloy-rich patches appear at the center position of groove. These observations clarified that the first molten droplet primarily conditions groove geometry changing because of the molten droplet dripping phenomenon.

Fig. 14(a ~ h) illustrated the transient evolution of the molten pool

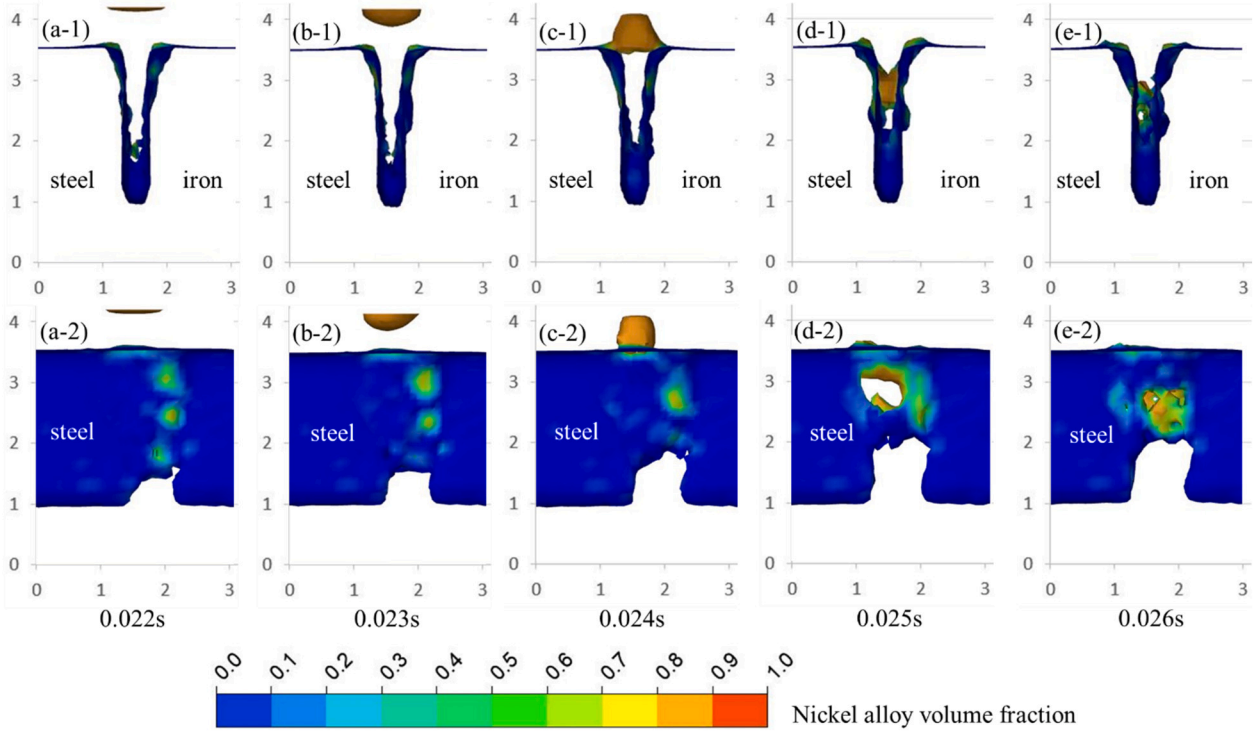

Fig. 13. The first molten droplet transfer progress in groove (a-1) ~ (e-1) Transverse section view (a-2) ~ (e-2) Longitudinal section view.

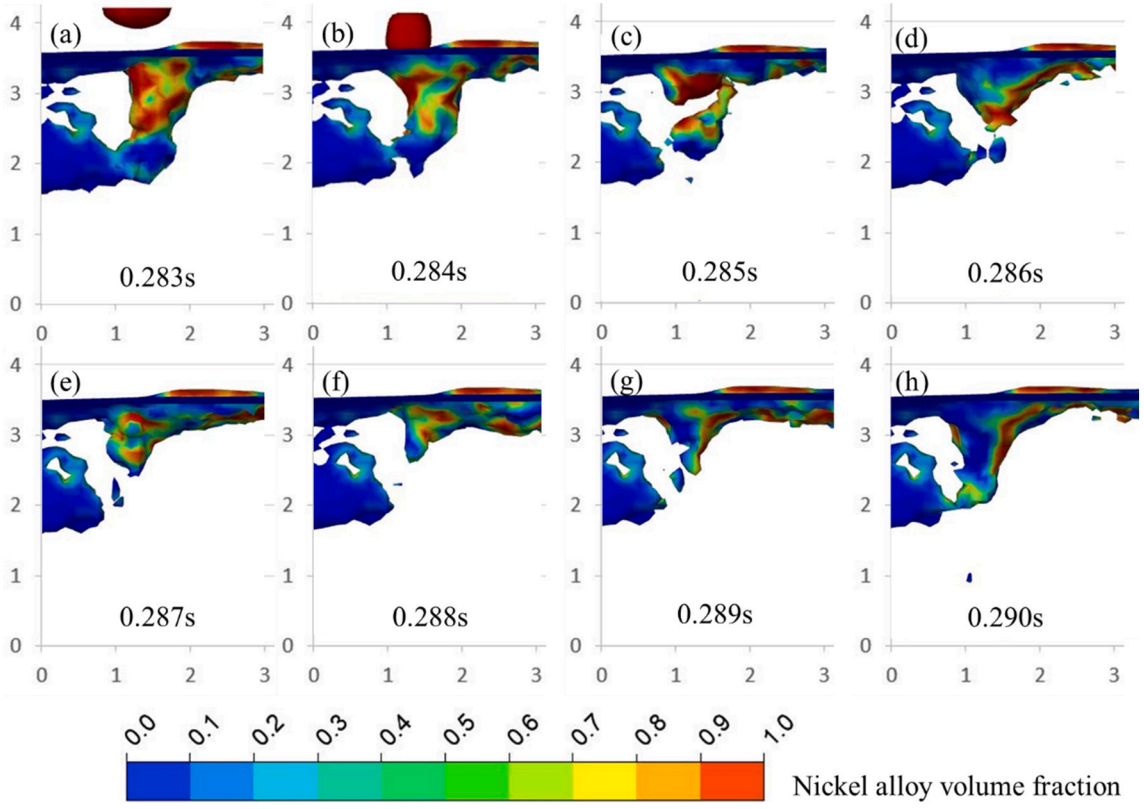

Fig. 14. Transient process of molten droplet transfer and material mixing during welding.

and keyhole during the transfer of a molten droplet at keyhole formation procedure. When the molten droplet entered the molten pool and contacted the keyhole wall surface, its relatively lower temperature led to a temporary cooling effect in the keyhole region. As a result, the local vapor induced recoil pressure at the keyhole bottom decreased, breaking the balance that sustained the keyhole cavity. Consequently, the keyhole became unstable and partially collapsed from the middle position, trapping a portion of vapor inside the molten pool and forming a

transient gas cavity, as shown in Fig. 14(c ~ d). Subsequently, the entrapped gas bubble rose upward and merged with the upper keyhole driven by buoyancy, releasing the trapped vapor. During this period, the keyhole depth decreased while the opening diameter becomes larger, reflecting a transition from a slender to a shallow–wide morphology shown in Fig. 14(e ~ f). As laser irradiation continued, the molten pool temperature increased again, enhancing evaporation at the keyhole bottom. Recoil pressure recovered and dominated the key role leading to the reformation of a deeper, elongated keyhole structure shown in Fig. 14(g ~ h).

In the longitudinal section, the distribution of the nickel-alloy component revealed clear asymmetry caused by surface tension gradient. The Marangoni flow drove the molten nickel-alloy from the front wall toward the rear wall of the molten pool. Consequently, a higher nickel-alloy concentration appeared along the rear surface, while the front side remained relatively less. This directional flow not only promoted the mixing between the filler and base metals but also reflected the strong coupling among surface tension, temperature gradient, and pool convection during dissimilar laser keyhole welding.

4.4. Velocity field in molten pool

Fig. 15(a ~ h) showed the velocity field on a transverse cross-section that was located just behind the keyhole, illustrating the evolution of molten metal flow during molten droplet transfer. Before the molten droplet entered the molten pool, the flow inside the molten pool was primarily governed by surface tension and recoil pressure shown in Fig. 15(a ~ b). Due to the temperature gradient along the free surface, the Marangoni flow drove the metal fluid toward the cast-iron side, producing an asymmetric circulation. The velocity vectors showed a strong vortex flow pattern, with the maximum velocity reaching approximately 0.5 m/s, which promoted the outward expansion of the upper molten pool and the widening of the keyhole opening.

After the molten droplet dripped into the molten pool shown in Fig. 15(c ~ d), the previous flow equilibrium was disrupted. The molten droplet metal (nickel-alloy) mixed rapidly with the pool metal, altering the temperature distribution. As a result, the temperature gradient between the two sides of the pool was temporarily reduced, weakening the Marangoni effect. The flow velocity decreased to about 0.25–0.3 m/s, and the vortices on both sides become more symmetric around the pool centerline.

With continued mixing and heat transfer shown in Fig. 15(f ~ h), the molten droplet material became fully mixed into the molten pool. The temperature field gradually recovered its original nonuniform distribution. Consequently, the Marangoni-driven convection made its asymmetry, and the molten metal flow pattern returned to a state like that in Fig. a, characterized by stronger flow toward the cast-iron side and an asymmetric vortex structure.

This cyclic evolution of the flow—from asymmetric to symmetric and back to asymmetric—reflected the strong coupling between thermal gradients, surface tension forces, and transient mixing induced by molten droplet transfer. The results highlighted that the instantaneous thermal and flow field disturbances introduced by the molten droplet play a crucial role in determining keyhole stability and the distribution of nickel-alloy in dissimilar metal welding.

4.5. Metal distribution

Fig. 16 showed the evolution of the three-metal distribution near the keyhole from 0.06 s to 0.48 s during laser welding. Since this section remained at the keyhole position, the welding time corresponded only to different spatial locations along the weld path, rather than real-time changes at a single point. Therefore, the following analysis reflected spatial variations in steady-state welding conditions.

At the early stage, melting occurred mainly along the interface between carbon steel and cast iron, forming a narrow molten layer at the bottom of groove. As laser moved forward, the molten pool expanded and keyhole formed, the interfacial mixing between the two base metals became stronger under strong Marangoni convection. Throughout the process, only a small portion of the nickel-alloy filler participates in

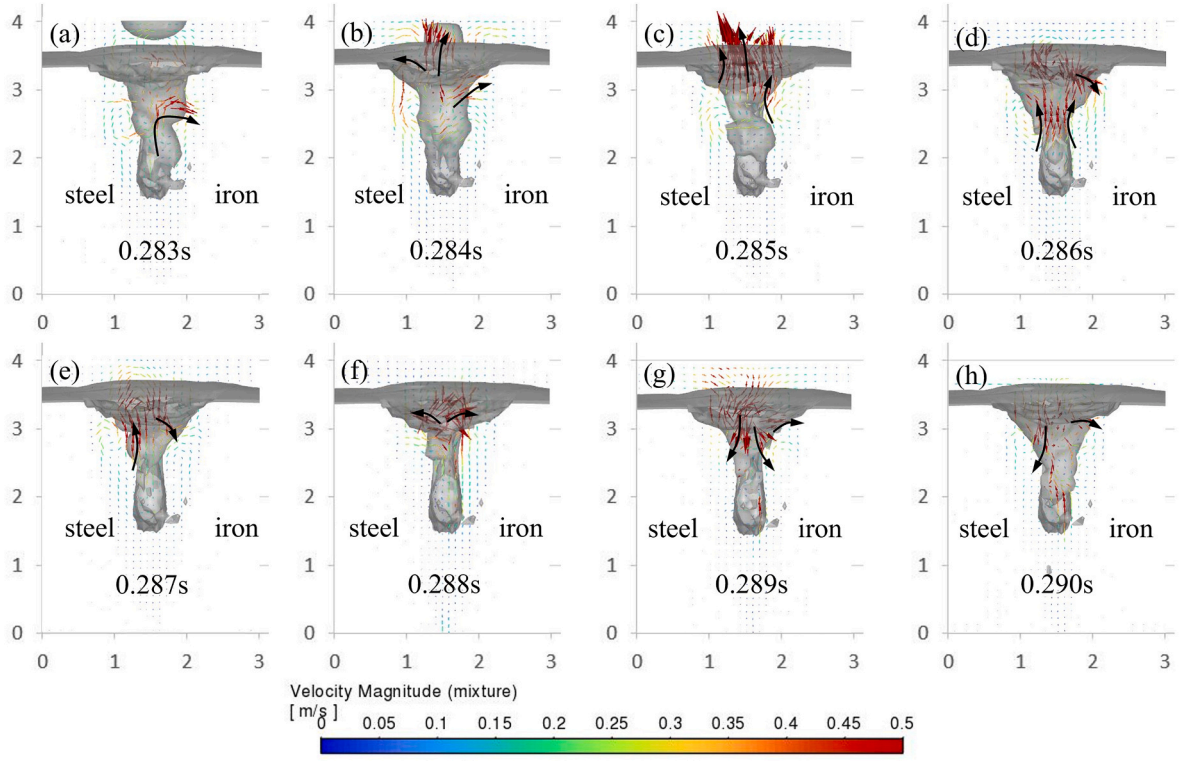

Fig. 15. Velocity distribution on transverse cross section.

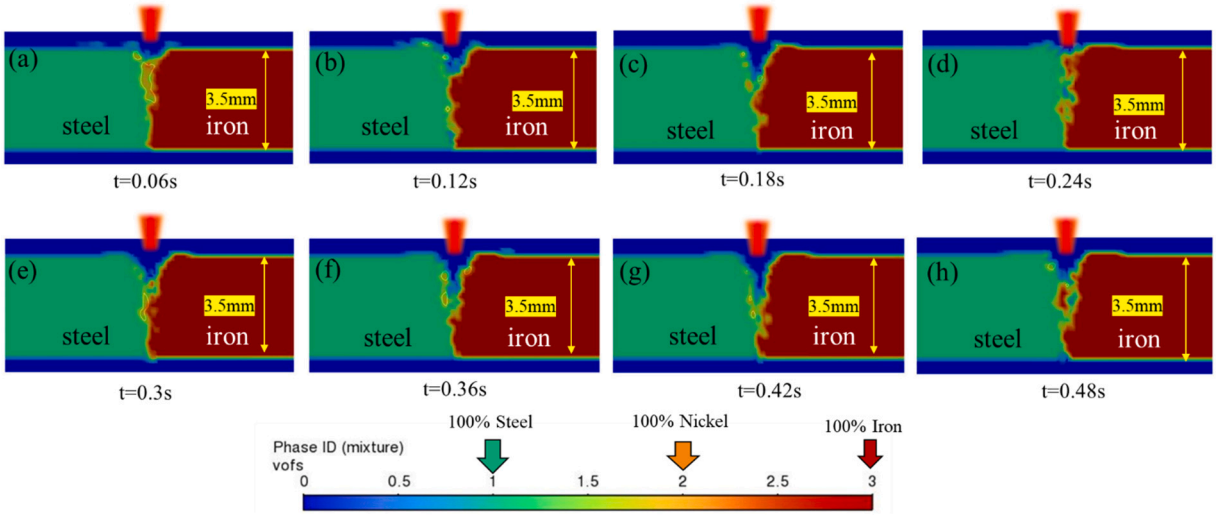

Fig. 16. Evolution of keyhole shape and material distribution at the laser irradiation position.

mixing and remains concentrated near the upper pool region, indicating limited diffusion compared with the Fe-based metals at keyhole position.

Fig. 17 illustrated the longitudinal distribution of the nickel-alloy at different concentration levels. The region before the yellow dashed line corresponded to the solidified zone, where the molten metal has completely solidified and no further flow occurred, as confirmed by the final solid–liquid interface shown in Fig. 17(h). The results indicated that the nickel-alloy was primarily concentrated in the upper half of the molten pool, where the flow intensity was strong and the influence of the keyhole and surface convection was most referred.

Quantitatively, more than 70 % of the total nickel-alloy volume fraction distributed within the upper 2.5 mm of the molten pool, while less than 10 % remained below the mid-depth region. The local volume fraction of nickel-alloy in the upper molten zone reached approximately 0.35–0.45, compared with only 0.05–0.15 near the pool bottom. This gradient demonstrated the strong upward transport of nickel-alloy driven by Marangoni convection and recoil-pressure-induced circulation near the keyhole. As the molten pool began to solidify, these flow paths gradually blocked, and the nickel-alloy distribution became fixed. No continuous region with 100 % nickel-alloy composition was observed, confirming that the filler material has been thoroughly mixed with the base metals. The resulting interfacial zone showed a smooth transition in composition rather than sharp phase separation. This mixed layer, with an average nickel-alloy content of about 20–25 %, served as a metallurgical bridge between carbon steel and cast iron, improving interfacial bonding while minimizing compositional segregation in the final joint. Overall, the nickel-alloy exhibited a gradient distribution along the vertical direction, with higher concentrations in the upper molten region and lower concentrations toward the bottom. This pattern results from the combined effects of surface-driven flow, keyhole dynamics, and progressive solidification. The final composition field suggested that the nickel-alloy effectively enhances the metallurgical bonding between carbon steel and cast iron by forming a uniformly mixed interfacial zone.

Fig. 18 showed the simulated prediction in the distributions of nickel-alloy within transverse cross section of the molten pool. The results exhibited a similar pattern, with nickel-alloy predominantly concentrated in the upper half of the fusion zone and a gradual decrease in concentration toward the bottom.

The simulation results indicated that approximately 65–75 % of the total nickel-alloy volume fraction distributed within the upper 60 % of the molten pool height, while less was found below mid-depth. This distribution is due to the combined effects of Marangoni convection, recoil-pressure-driven upward flow near the keyhole front, and the solidification sequence that causes nickel-alloy to remain in the last-

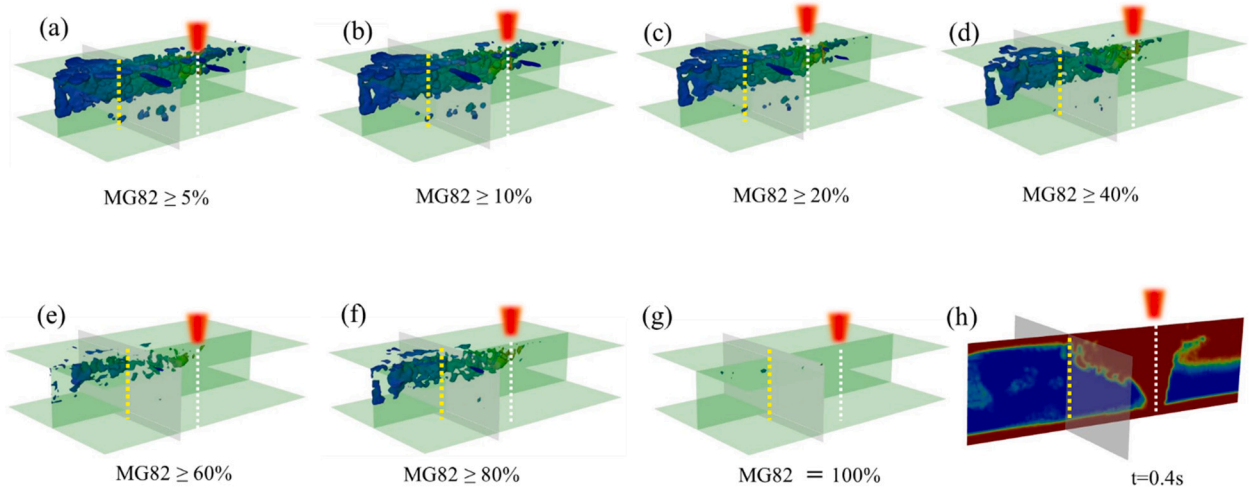

Fig. 17. Longitudinal distribution of the nickel-alloy at different concentration levels from 5 % ~ 100 %.

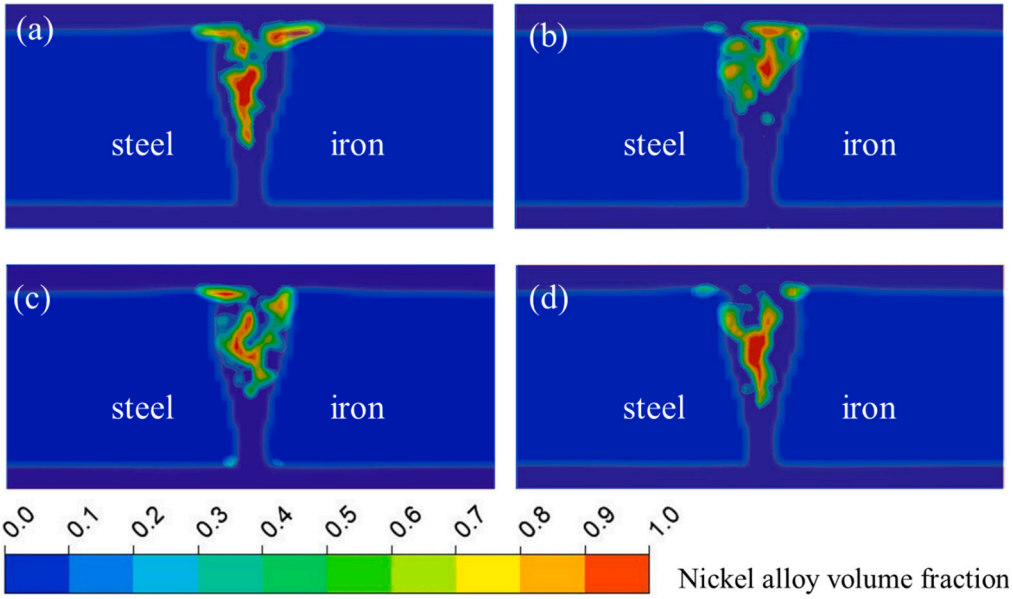

Fig. 18. Similar distribution of nickel-alloy at different transverse cross sections.

solidifying regions near the surface.

At higher laser power and shallower focus positions, simulation results showed a wider spread of nickel-alloy across the pool surface, whereas deeper focus or lower power results in more localized Ni enrichment. These findings suggested that the molten pool flow pattern and keyhole depth directly influence the extent of nickel-alloy dispersion, and optimizing laser power and focal position can improve the homogeneity of filler metal distribution.

5. Conclusions

A three-dimensional CFD model was developed to simulate dissimilar keyhole laser welding of carbon steel and cast iron with a nickel-alloy filler wire. The model successfully captured the main physical phenomena including molten droplet transfer, molten pool morphology, temperature field and nickel-alloy distribution in the molten pool. The conclusions are summarized as follows:

(1) The keyhole exhibited periodic opening and collapse behavior due to the dynamic balance between recoil pressure and surface tension. During collapse, transient gas bubbles were generated but subsequently released through buoyancy-driven motion.
(2) The asymmetric flow pattern in molten pool due to laser welding dissimilar materials is dominant. When molten wire droplets transferred into molten pool with keyhole, the flow pattern and local temperature field changed significantly. It temporarily reduced the temperature gradient and Marangoni-driven asymmetric flow. With the progress of the mixing of molten wire droplets with two dissimilar base metals, the asymmetric flow pattern reappeared.
(3) The nickel-alloy was primarily distributed in the upper half region of the molten pool and its volume fraction was around 65 %–75 %. The nickel-alloy filler metal was well mixed with the base metals of cast iron and carbon steel, forming a graded transition layer with 20–25 % nickel-alloy content that enhanced metallurgical bonding and compositional uniformity in the welded metal.

CRediT authorship contribution statement

Renzhi Zhang: Writing – original draft, Validation, Methodology, Investigation. **Daichi Nishimoto:** Validation, Investigation. **Ninshu Ma:** Writing – review & editing, Supervision, Software, Resources, Conceptualization. **Fenggui Lu:** Validation. **Tetsuo Suga:** Resources. **Takayuki Tabuchi:** Resources. **Syuichi Shimada:** Resources.

Declaration of competing interest

There is no conflict of interest in this paper.

Acknowledgement

This work was partially supported by “Osaka University promotion program of cutting-edge multilateral international collaboration related to joining and materials science” and “JWRI International Joint Research Collaborators (JIJReC) program”.

The author would like to express sincere gratitude to the engineers at JATCO Co., Ltd. for their generous assistance in providing experimental data and technical insights.

Appreciation is also extended to Professor Qian Wang for her guidance during the early stages of this study, and to Dr. Wenjia Huang and Dr. Yang Li for their technical support and helpful discussions.

References

[1] Quazi MM, Ishak M, Fazal MA, Arslan A, Rubaiee Saeed, Aiman MH, et al. A comprehensive assessment of laser welding of biomedical devices and implant materials: recent research, development and applications. Crit Rev Solid State Mater Sci 2020;46:109–51.
[2] Khan MS. Recent advances in mitigating fusion zone softening during laser welding of Al-Si coated 22MnB5 press-hardened steels. Mater Res Express 2023:10. https://doi.org/10.1088/2053-1591/acead5.
[3] Ceglarek D, Colledani M, Váncza J, Kim DY, Marine C, Kogel-Hollacher M, et al. Rapid deployment of remote laser welding processes in automotive assembly systems. CIRP Ann Manuf Technol 2015;64:389–94. https://doi.org/10.1016/j.cirp.2015.04.119.
[4] Hong KM, Shin YC. Prospects of laser welding technology in the automotive industry: a review. J Mater Process Technol 2017;245:46–69. https://doi.org/10.1016/j.jmatprotec.2017.02.008.
[5] Fourkas JT, Sugioka K, Lu Y. Editorial: Frontiers in lasers and applications. Front Nanotechnol 2024:6. https://doi.org/10.3389/fnano.2024.1371102.
[6] Jauregui-Cervantez RE, Flores-Preciado JC, García-Gallegos JC, Soto-Tapiz MI. Bioengineering: an alternative technological innovation for the use of dental laser. EAS J Dent Oral Med 2023;5:180–4. https://doi.org/10.36349/easjdom.2023.v05i06.006.
[7] Khan MS, Ali S, Westerbaan D, Duley W, Biro E, Zhou YN. The effect of laser impingement angle on the optimization of melt pool geometry to improve process

stability during high-speed laser welding of thin-gauge automotive steels. J Manuf Process 2022;78:242–53. https://doi.org/10.1016/j.jmapro.2022.04.022.
[8] Liu W, Ma J, Liu S, Kovacevic R. Experimental and numerical investigation of laser hot wire welding. Int J Adv Manuf Technol 2015;78:1485–99. https://doi.org/10.1007/s00170-014-6756-9.
[9] Jiménez-Xamán M, Hernández-Hernández M, Tariq R, Landa-Damas S, Rodríguez-Vázquez M, Aranda-Arizmendi A, et al. Numerical simulations and mathematical models in laser welding: a review based on physics and heat source models. Front Mech Eng 2024:10. https://doi.org/10.3389/fmech.2024.1325623.
[10] Hu S, Li F, Zuo P. Numerical simulation of laser transmission welding—a review on temperature field, stress field, melt flow field, and thermal degradation. Polymers (Basel) 2023:15. https://doi.org/10.3390/polym15092125.
[11] Dal M, Fabbro R. An overview of the state of art in laser welding simulation. Opt Laser Technol 2016;78:2–14 [INVITED], https://doi.org/10.1016/j.optlastec.2015.09.015.
[12] Chang WS, Na SJ. A study on the prediction of the laser weld shape with varying heat source equations and the thermal distortion of a small structure in micro-joining $. n.d.
[13] Kik T. Heat source models in numerical simulations of laser welding. Materials 2020:13. https://doi.org/10.3390/ma13112653.
[14] Behúlová M, Babalová E. Heat source models for numerical simulation of laser welding processes - a short review. J Phys Conf Ser 2024;2712. https://doi.org/10.1088/1742-6596/2712/1/012018. Institute of Physics.
[15] Lin R, Wang, Ping H, Lu F, Solomon J, Carlson BE. Numerical study of keyhole dynamics and keyhole-induced porosity formation in remote laser welding of Al alloys. Int J Heat Mass Transf 2017;108:244–56. https://doi.org/10.1016/j.ijheatmasstransfer.2016.12.019.
[16] Huang S, Xu L, Lou M, Chen H, Zhang K, Li Y. Keyhole-induced pore formation mechanism in laser-MIG hybrid welding of aluminum alloy based on experiment and multiphase numerical model. J Mater Process Technol 2023:314. https://doi.org/10.1016/j.jmatprotec.2023.117903.
[17] Eriksson I, Gren P, Powell J, Kaplan AF. New high-speed photography technique for observation of fluid flow in laser welding. Opt Eng 2010;49:1. https://doi.org/10.1117/1.3502567.
[18] Feng J, Zhang P, Yan H, Shi H, Lu Q, Liu Z, et al. Application of laser welding in electric vehicle battery manufacturing: a review. Coatings 2023:13. https://doi.org/10.3390/coatings13081313.
[19] Jung SH, Kim HJ. Application of laser welding to STS301L side structure of railway vehicles(I) - vertical incidence welding conditions for laser beam based on multiple regression analysis. J Mech Sci Technol 2023;37:3087–94. https://doi.org/10.1007/s12206-023-0532-4.
[20] Farhadipour P, Omidi N, Barka N, Nadeau F, Idriss M, El Ouafi A. Systematic approach to improve overlap laser welding of AA5052-H32 with dissimilar thickness by evaluation of mechanical performance, undercut, and welding penetration. Int J Adv Manuf Technol 2024;130:3387–99. https://doi.org/10.1007/s00170-023-12872-2.
[21] Wang P, Chen X, Pan Q, Madigan B, Long J. Laser welding dissimilar materials of aluminum to steel: an overview. Int J Adv Manuf Technol 2016;87:3081–90. https://doi.org/10.1007/s00170-016-8725-y.
[22] Rossini M, Spena PR, Cortese L, Matteis P, Firrao D. Investigation on dissimilar laser welding of advanced high strength steel sheets for the automotive industry. Mater Sci Eng A 2015;628:288–96. https://doi.org/10.1016/j.msea.2015.01.037.
[23] Li P, Fan Y, Zhang C, Zhu Z, Tian W, Liu A. Research on heat source model and weld profile for fiber laser welding of A304 stainless steel thin sheet. Adv Mater Sci Eng 2018:2018. https://doi.org/10.1155/2018/5895027.
[24] Yan S, Li Z, Song L, Zhang Y, Wei S. Research and development status of laser micro-welding of aluminum-copper dissimilar metals: a review. Opt Lasers Eng 2023:161. https://doi.org/10.1016/j.optlaseng.2022.107312.
[25] Huang W, Wang H, Rinker T, Tan W. Investigation of metal mixing in laser keyhole welding of dissimilar metals. Mater Des 2020:195. https://doi.org/10.1016/j.matdes.2020.109056.
[26] Ai Y, Dong G, Yuan P, Liu X, Yan Y. The influence of keyhole dynamic behaviors on the asymmetry characteristics of weld during dissimilar materials laser keyhole welding by experimental and numerical simulation methods. Int J Therm Sci 2023;190. https://doi.org/10.1016/j.ijthermalsci.2023.108289.
[27] Shehryar Khan M, Shahabad SI, Yavuz M, Duley WW, Biro E, Zhou Y. Numerical modelling and experimental validation of the effect of laser beam defocusing on process optimization during fiber laser welding of automotive press-hardened steels. J Manuf Process 2021;67:535–44. https://doi.org/10.1016/j.jmapro.2021.05.006.
[28] Wu D, Ishida K, Tashiro S, Nomura K, Hua X, Ma N, et al. Dynamic keyhole behaviors and element mixing in paraxial hybrid plasma-MIG welding with a gap. Int J Heat Mass Transf 2023:200. https://doi.org/10.1016/j.ijheatmasstransfer.2022.123551.
[29] Geng R, Ma N, Nishimoto D, Zhang R, Lu F, Li Z. Microstructure, element distribution and interfacial properties of laser welded iron–nickel–steel dissimilar joints. J Mater Res Technol 2025;37:2463–73. https://doi.org/10.1016/j.jmrt.2025.06.152.
[30] Zhang R, Nishimoto D, Ma N, Narasaki K, Wang Q, Suga T, et al. Asymmetric molten zone and hybrid heat source modeling in laser welding carbon steel and cast iron with nickel alloy wires. J Manuf Process 2025;142:177–90. https://doi.org/10.1016/j.jmapro.2025.03.074.
[31] I Brown OL. The Clausius-Clapeyron equation. 2025.
[32] Tong LG, Gu JC, Yin SW, Wang L, Bai SW. Impacts of torch moving on phase change and fluid flow in weld pool of SMAW. Int J Heat Mass Transf 2016;100:949–57. https://doi.org/10.1016/j.ijheatmasstransfer.2016.04.032.
[33] Tong LG, Gu JC, Wang L, Yin SW. Influences of deposited metal material parameters on weld pool geometry during shield metal arc welding. Int J Heat Mass Transf 2015;90:968–78. https://doi.org/10.1016/j.ijheatmasstransfer.2015.06.051.
[34] Fan HG, Tsai HL, Na SJ. Heat transfer and ¯uid ¯ow in a partially or fully penetrated weld pool in gas tungsten arc welding. n.d.